Supplementary Information (SI) for Journal of Materials Chemistry A.

Electronic Supplementary Information

Enhancing Zinc-Ion Energy Storage: Impact of MOF-5 Derived Carbonization Temperature on Performance

Wojciech Kukułka, Verónica Montes-García, Saira Sarwar, Dawid Pakulski, Paolo Samorì, Artur Ciesielski**

Table of Contents

Section A. Materials and methods

Materials

Zinc nitrate hexahydrate ($Zn(NO_3)_2 \cdot 6H_2O$), zinc foil, terephthalic acid ($C_6H_4(COOH)_2$) and N-Methyl-2-pyrrolidone (NMP) were bought from Sigma Aldrich. N,N–dimethylformamide (DMF) was purchased from CARLO ERBA (France) and zinc trifluoromethanesulfonate ($Zn(CF_3SO_3)_2$ or $Zn(OTf)_2$) was purchased from Tokyo Chemical Industry (TCI, Japan). Polyvinylidene fluoride (PVDF) binder, conductive carbon black (Super P – SP) and activated carbon (AC) were bought from Alfa Aesar (Germany).

Synthesis and carbonization of MOF-5

The synthesis of MOF-5 was based on a previously reported procedure.[1,2] Briefly, a solution was prepared by dissolving zinc nitrate tetrahydrate (982 mg, 3.75 mmol) and terephthalic acid (299 mg, 1.8 mmol) in 360 mL of DMF. The solution was then stirred at 110 ˚C for 48 hours. After this time, the solution was centrifuged at 8,000 rpm for 10 minutes to obtain a white powder. For its subsequent carbonization, the resulting powder was placed in a ceramic boat in a tube furnace, initially heated to 110 ˚C to remove residual solvent from the pores, and then heated to the desired temperature (600-1000 ˚C), maintained for two hours, and then cooled down to room temperature. The entire process was carried out under an inert argon atmosphere. Along the manuscript and ESI the samples will be denoted as CMOF-5_X, being X the carbonization temperature.

Methods

The morphology and surface structure of the samples were investigated by **scanning electron microscopy (SEM**), using a Quanta 250 FEG, FEI. Specific surface area and total pore volume were analyzed through nitrogen adsorption/desorption isotherms, using the **Brunauer, Emmett and Teller (BET**) model and Density Functional Theory (DFT), and was performed with an ASAP 2050 (Micromeritics). **X-ray diffraction (XRD)** patterns were carried out using D8 Bruker Diffractometer with Cu lamp (Kα1 = 1.5418 Å) to determine the crystal structure and phase composition of the samples. **Thermogravimetric analysis (TGA)** was performed using the TGA/DSC 2 (Mettler Toledo) instrument at the heating rate of 10 °C/min from room temperature to 1000 °C in air to study the thermal stability and mass loss of the samples. **Raman** spectra were recorded using Via Raman Microscope (Renishaw) with the excitation wavelength of 532 nm to provide information on the vibrational modes of the samples. **X-ray Photoelectron Spectroscopy (XPS**) analyses were performed with a K-Alpha X-ray photoelectron spectrometer (Thermo Scientific) equipped with an aluminum X-ray source (energy 1.4866 keV), operating at a vacuum level of 10^{-8}-10^{-9} mbar in the main chamber. The spot size of the X-ray beam was fixed at 400 μm. XPS was used to determine the chemical composition and surface chemistry of the samples.

Probe station measurements. Electrical conductivity measurements were conducted on films of different materials. Ag paste was used to connect the samples to the probe station. The electrical conductivity of the pellets was measured with a probe station, under ambient conditions, using a Keithley 2626A SourceMeter unit. The IV curves were recorded by sweeping the voltage from 0 to 2 V and from 2 to 0 V.

The electrical conductivity (σ) was estimated using the following equation

$$\sigma = {}^{L}\!/_{(R \cdot W \cdot t)} \tag{1}$$

Where R is the measured resistance, L is the length, W the width and t is thickness of the film.

Electrode fabrication

Electrochemical measurement configuration

Two-electrode system: The electrochemical measurements were performed in a two-electrode system using a measuring cell containing a cathode (*i.e.,* CMOF-5 or AC) and an anode (*i.e.,* zinc foil) separated by glassy fibrous paper (Whatman GF/G) soaked with 3 M $Zn(CF_3SO_3)_2$ aqueous electrolyte. The cathode electrode is composed of 70 wt.% of CMOF-5_X, 20 wt.% of Super P. conductive carbon, and 10 wt.% of polytetrafluoroethylene (PVDF) as the binder. The two-electrode system was enclosed in a CR2032-type cells. The average mass loading of active material was ~1 mg per electrode (~2 mg/cm^2), with an active layer thickness of approximately 100 μm, corresponding to a compaction density of ~0.2 g/cm^3.

Electrochemical performance

The electrochemical performance of two-electrode systems was assessed using cyclic voltammetry (CV), and electrochemical impedance spectroscopy (EIS) on Autolab PGSTAT128N Potentiostat/Galvanostat instrument with a Metrohm Autolab DuoCoin Cell Holder (Metrohm AG) at room temperature. CV was performed at scan rates of 1 - 500 mV/s in the voltage range between 0 and 1.8 V. EIS measurements were recorded with a frequency range of 0.01 Hz to 1 MHz. The galvanostatic charge-discharge (GCD) tests were performed on Neware Battery Tester (BTS-4008T-5V/10mA, Neware Technology Company, China). GCD curves were tested at current densities ranging from 0.1 to 5 A/g.

Capacitance was calculated from the equation:

$$C = \frac{\int I(V)dV}{mv\Delta V} \tag{2}$$

Where: C: Specific capacitance (in F/g), i.e., capacitance normalized by mass of active material, m: Mass of active material in a single electrode (g), ΔV: Voltage window over which the CV is performed (V), v: Scan rate of the CV experiment (V/s), I(V): Current as a function of voltage (A), ∫I(V) dV: Area under the CV curve, representing the total current integrated over the voltage range (A·V).

Capacity was calculated from the equation:

$$Q = \frac{I\Delta t}{m3.6} \tag{3}$$

Where Q - capacity (mAh/g), I - current (A), Δt - discharge time (s) and m (g) is the mass of active material in 1 electrode.

Energy density was calculated from the equation:

$$Energy\ density = Capacity \times \Delta V \tag{4}$$

Where ΔV - voltage window.

Power density was calculated from the equation:

$$Power\ density = \frac{Energy\ density}{t} \tag{5}$$

Where power density (W/kg) and t (h) – discharge time.

Calculation of the capacitive/diffusion contribution:

$$i = av^b \tag{6}$$

$$\log i = a + b\log v \tag{7}$$

Where i is the current (A) and v is the scan rate (V/s).

Section B. Physical characterization

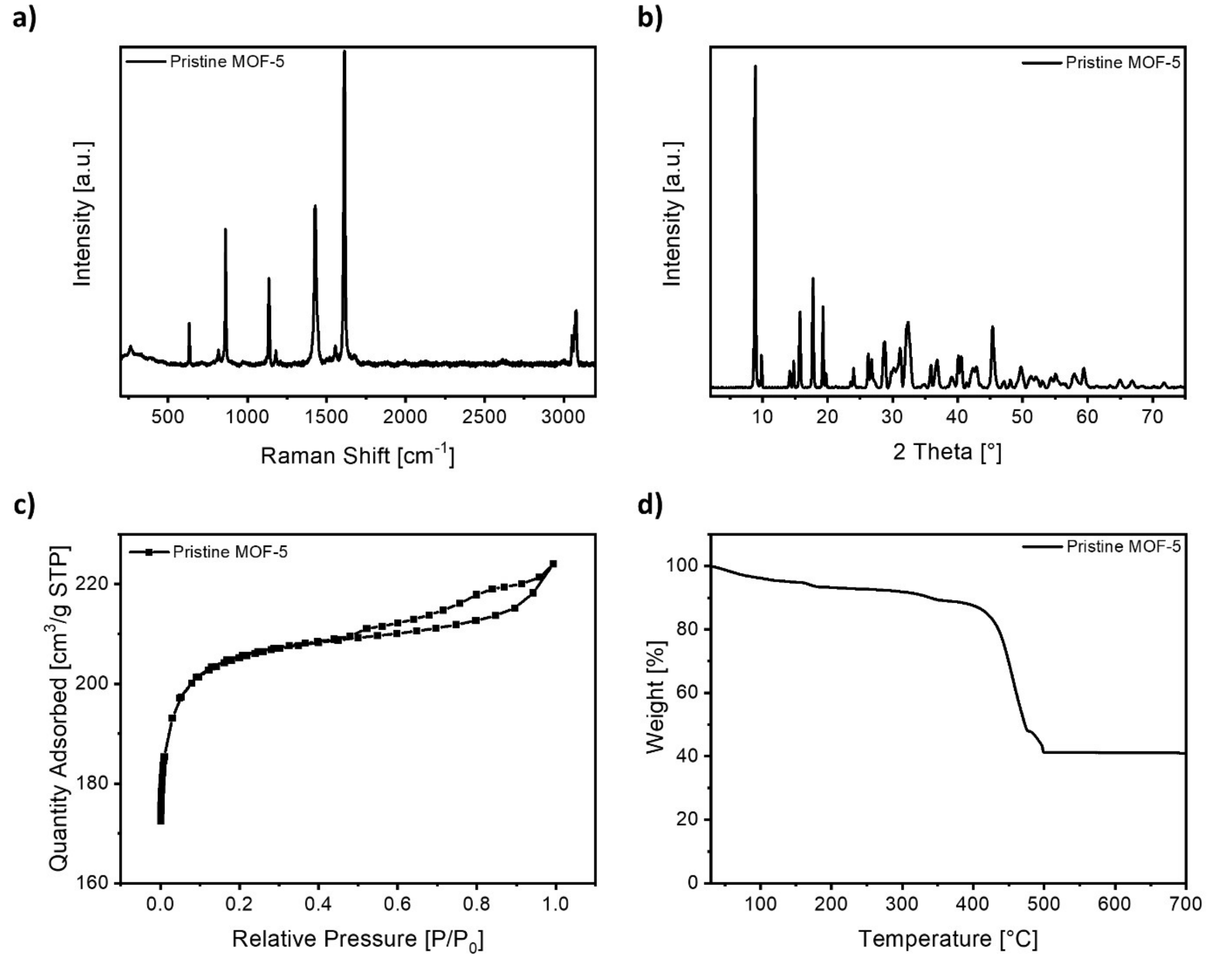

Fig. S1. a) Raman spectrum, b) PXRD, c) nitrogen adsorption/desorption isotherms, and d) TGA in air curve of pristine MOF-5.

Raman spectroscopy is employed to confirm the chemical composition of MOF-5 (Fig. S1a). Five major bands at 1615, 1433, 1140, 866 and 635 cm^{-1} are observed, corresponding to the vibrational modes of carboxylic group and aromatic benzene ring of the terephthalic acid ligand, in agreement with previous reports. The XRD pattern of pristine MOF-5 (Fig. S1b) reveals a close alignment between the diffraction peaks of the synthesized MOF-5 and the pattern reported previously for MOF-5, indicating the successful synthesis of the MOF-5 material.[3,4] The adsorption isotherms of MOF-5 exhibit type-I sorption isotherm, with steep rises appearing at a low relative pressure and type-IV sorption features with adsorption/desorption hysteresis at higher pressure. The calculated BET surface area of MOF-5 amounts to 631.03 ± 16.76 m^2/g (Fig. S1c) and the DFT total pore volume amounts to 0.26 cm^3/g. The thermal stability of pristine MOF-5, as assessed by TGA, is reported in Fig. S1d. It reveals a fast process with 45.5 % weight loss in the temperature range of 400–450 °C for the crystal MOF-5, which corresponds to its structure decomposition.

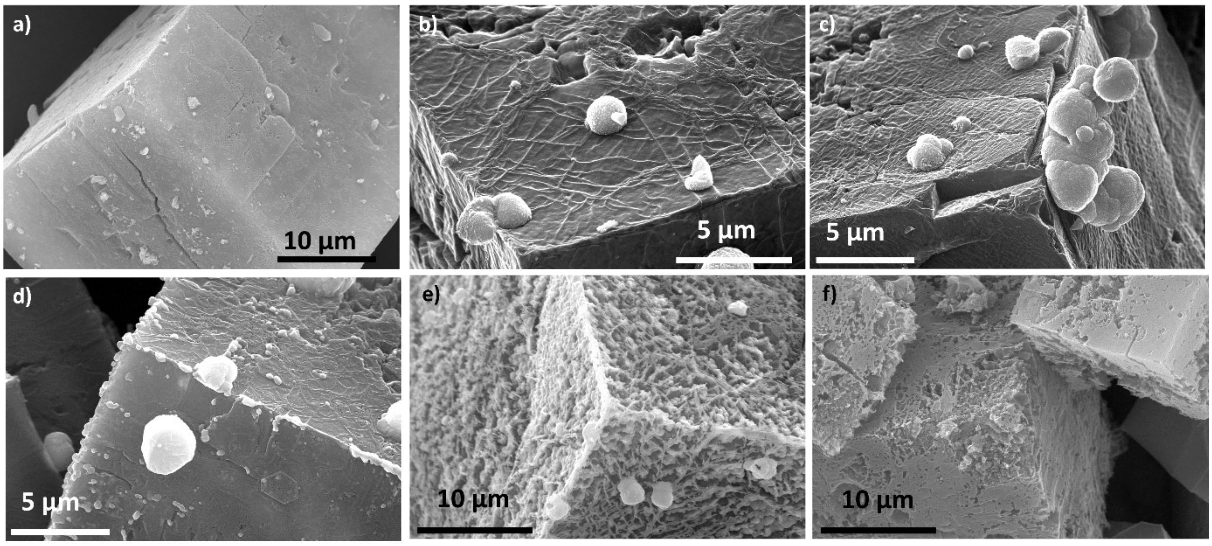

Fig. S2. High magnification of SEM images of a) MOF-5 and CMOF-5 carbonized at b) 600 °C, c) 700 °C, d) 800 °C, e) 900 °C and f) 1000 °C.

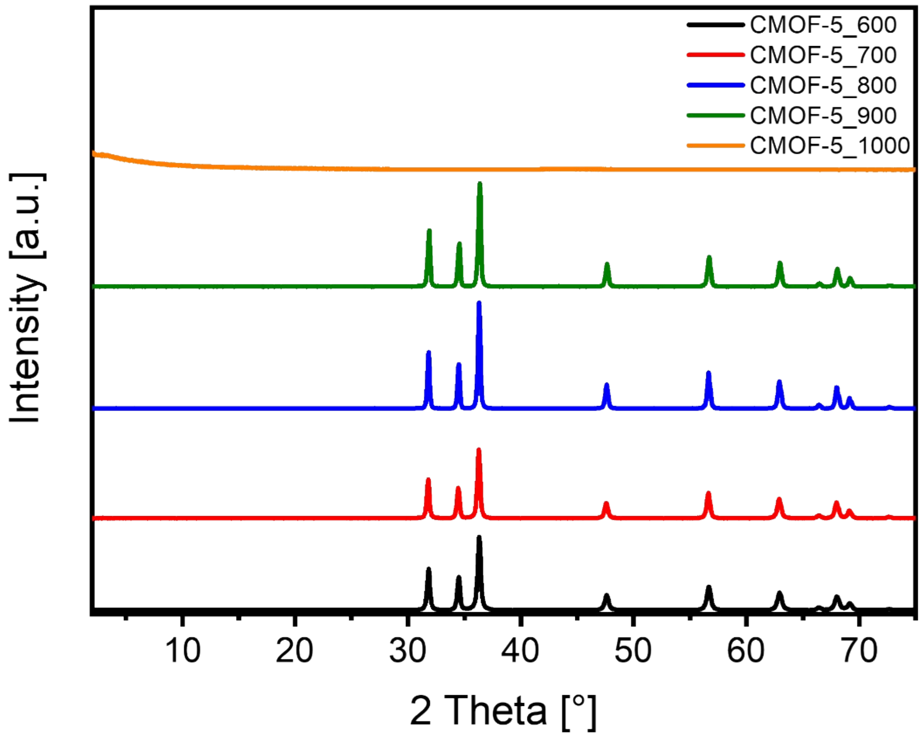

Fig. S3. XRD patterns of all CMOF-5 samples.

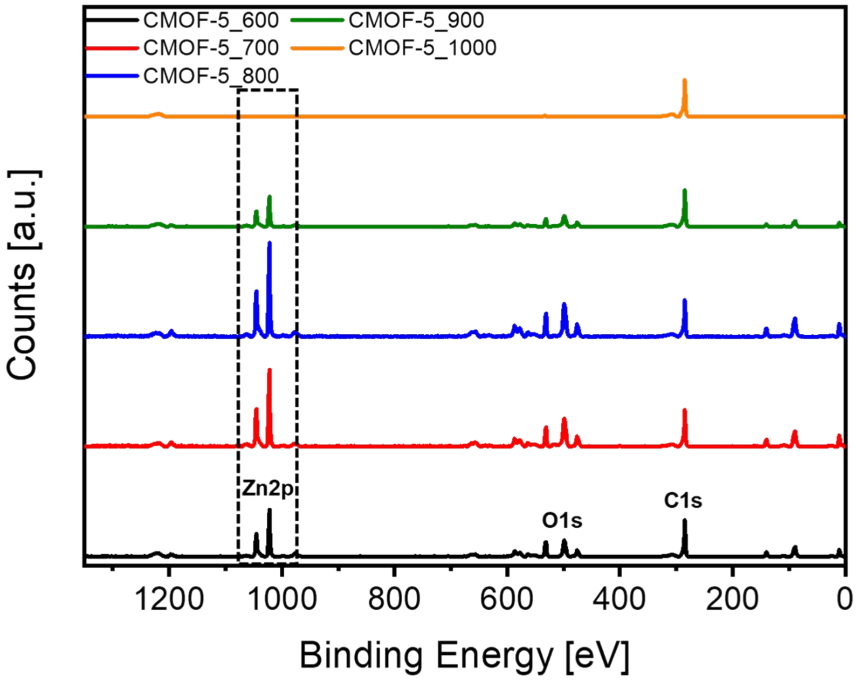

Fig. S4. XPS survey spectra of all CMOF-5 samples.

Table S1. Atomic contribution of elements on the surface in all CMOF-5 samples from XPS analysis.

Sample	**C [At. %]**	**O [At. %]**	**Zn [At. %]**	**Ratio C/Zn**	**Ratio Zn/O**
CMOF-5_600	76.9	14.7	8.4	9.15	0.57
CMOF-5_700	74.5	16.2	9.3	8.01	0.57
CMOF-5_800	69.6	16.6	13.8	5.04	0.83
CMOF-5_900	86.6	7.8	5.6	15.46	0.72
CMOF-5_1000	98.3	1.7	0.0	-	-

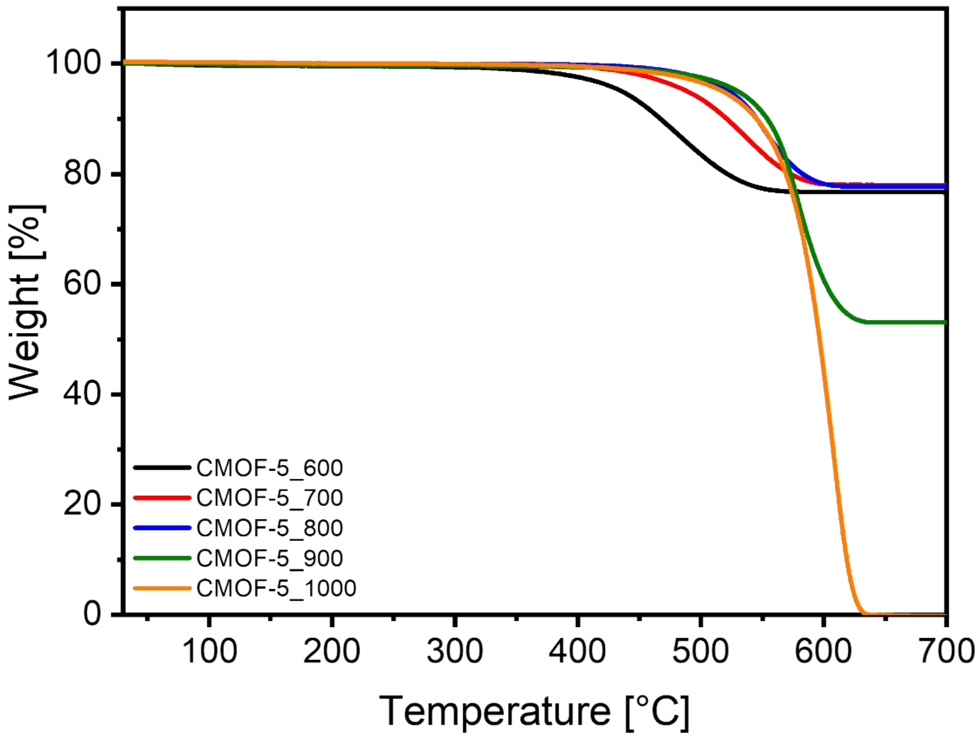

Fig. S5. TGA in air curves of all CMOF-5 samples.

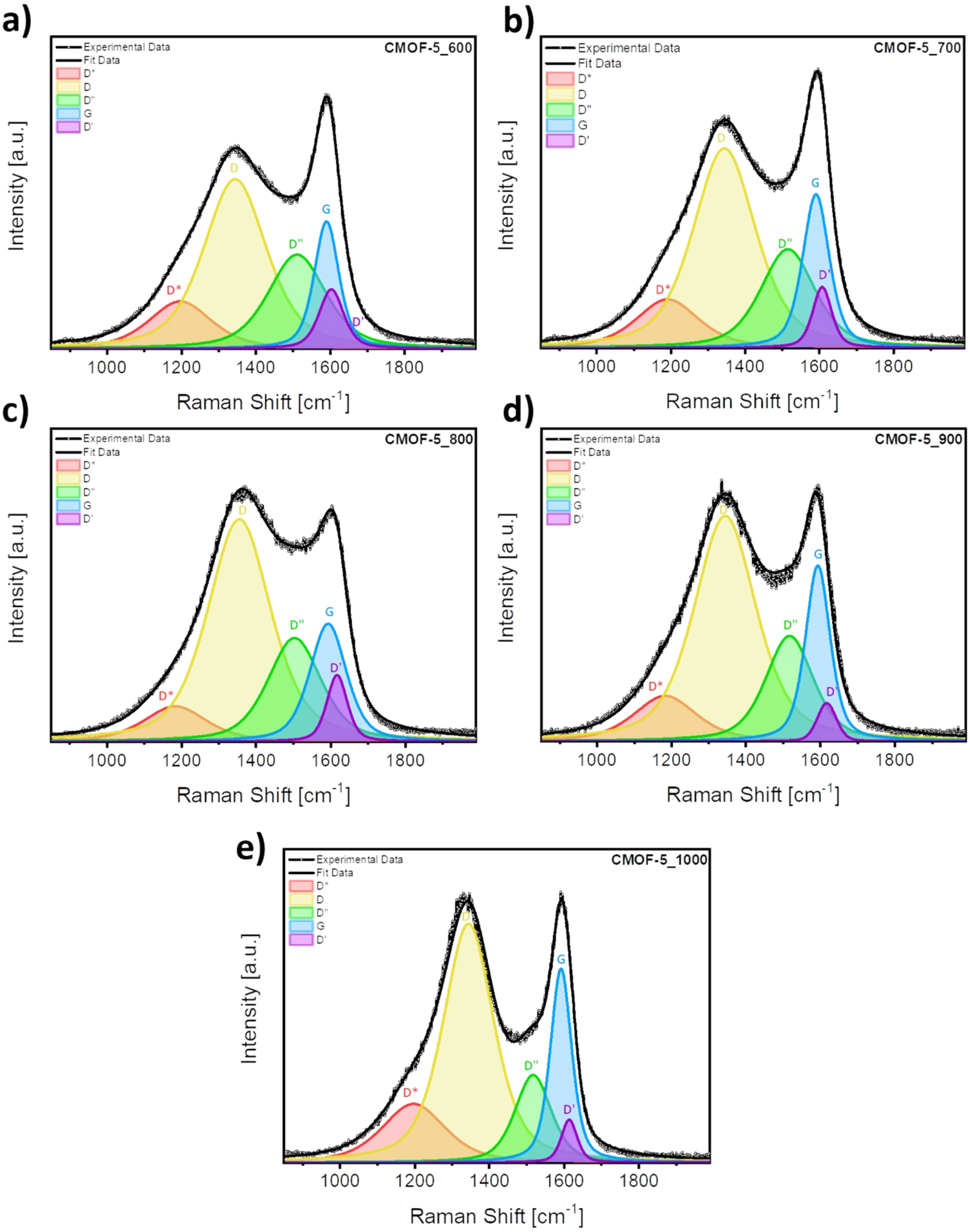

Fig. S6. Fitted Raman spectra of all CMOF-5 samples.

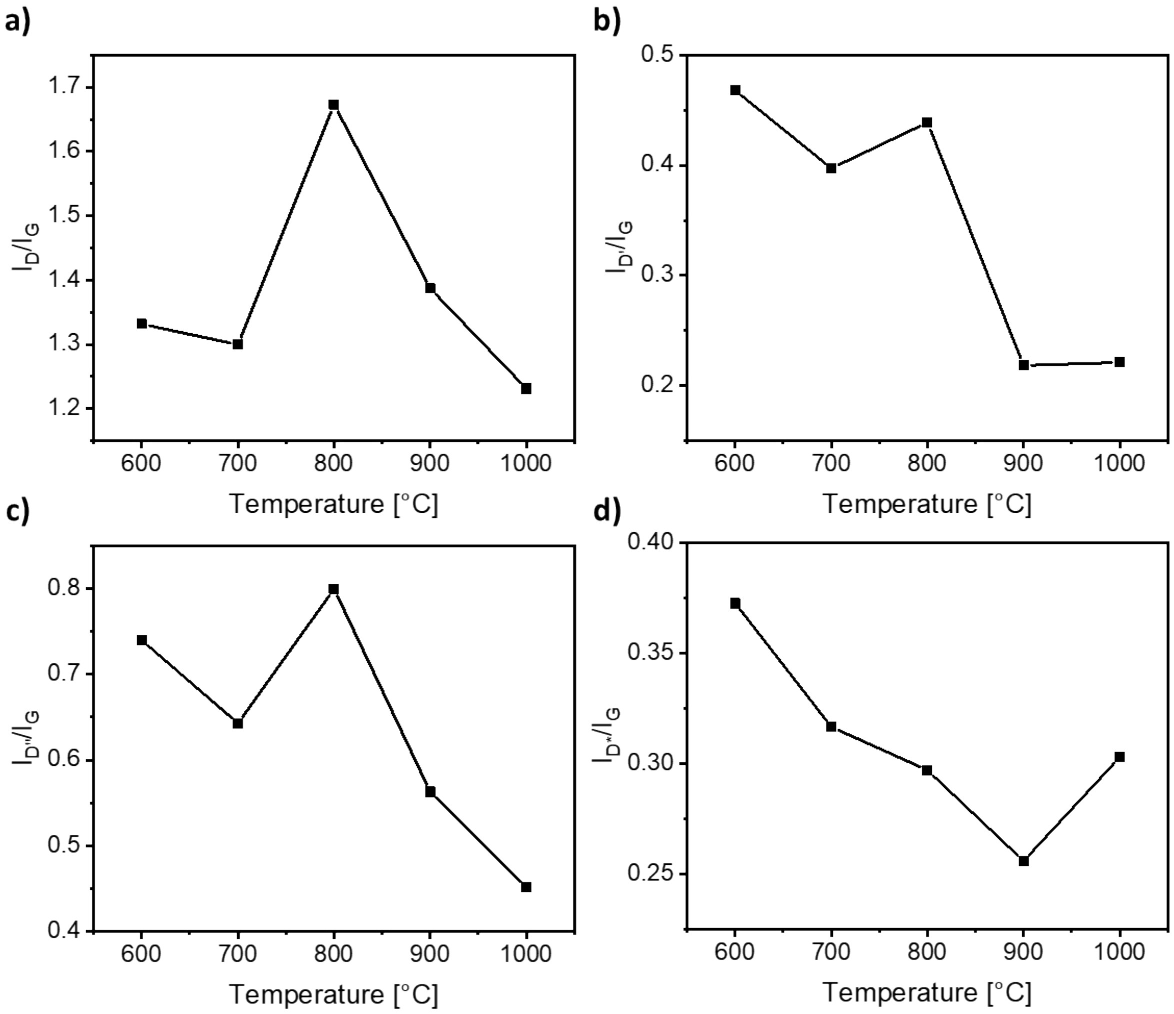

Fig. S7. Ratio of the band intensities a) I_D/I_G, b) $I_{D'}/I_G$, c) $I_{D''}/I_G$, d) I_{D*}/I_G of all CMOF-5 samples.

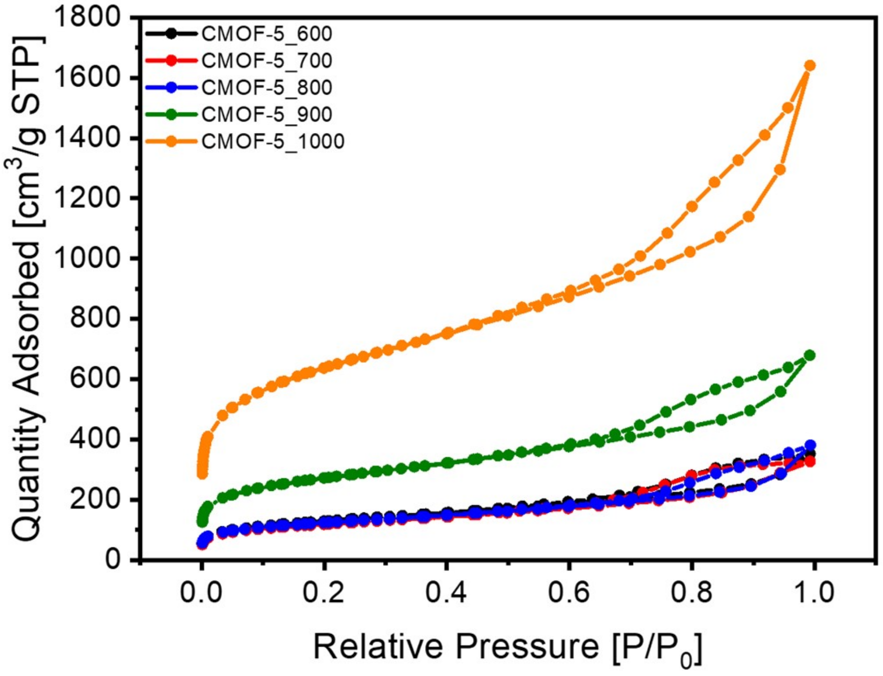

Fig. S8. Nitrogen adsorption/desorption isotherms of all CMOF-5 samples.

Table S2. Texture parameters of the all obtained CMOF-5 samples.

Sample	BET surface area [m^2/g]	Total pore volume [cm^3/g]
CMOF-5_600	443.80 ± 4.59	0.41
CMOF-5_700	404.86 ± 4.18	0.41
CMOF-5_800	420.12 ± 4.50	0.43
CMOF-5_900	919.06 ± 11.27	0.78
CMOF-5_1000	2151.07 ± 27.17	1.87

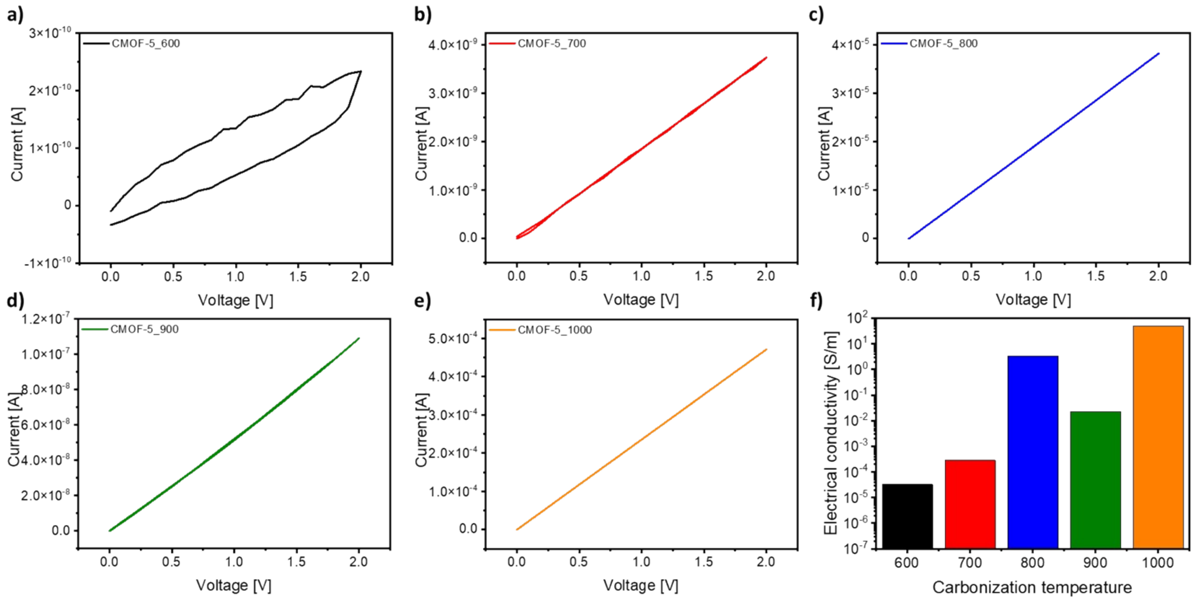

Fig. S9. a-e) IV curves and f) electrical conductivity of all CMOF-5 samples.

I-V curves are obtained by applying a sweeping voltage between 0 and 2 V and between 2 and 0 V for all the carbonized samples (Fig. S9a-e). Film conductivities are then estimated (see Experimental section for details) and reported in Figure S9f. The film's conductivity initially rises with the carbonization temperature, reaching a maximum at 800 ºC, followed by a decrease at 900 ºC, and subsequently, another increase at 1000 ºC. The observed trend can be linked to the variation in Zn and ZnO contents within the samples. Below 800 ºC, the predominant process involves the generation of ZnO, that migrates towards the surface of CMOF-5, resulting in an increase in electrical conductivity. However, at 800 ºC, the carboreduction of ZnO initiates, converting portions of ZnO into metallic Zn. The occurrence of this transformation is also evidenced by the Zn/O ratio evolution which is determined from the XPS survey spectra (Table S1). While this ratio amounts to 0.57 for samples treated at carbonization temperatures of 600 and 700 ºC, it rises up to 0.83 at 800 ºC, due to the emergence of metallic Zn, that also determines a substantial increase in conductivity. Subsequently, at 900 ºC, the evaporation of metallic Zn begins (as the approximated evaporation temperature of Zn is 907 ºC), leading to a reduction in the Zn/O ratio to 0.72. Consequently, as metallic elements depart from the CMOF-5 structure, the overall electrical conductivity decreases. Finally, at a carbonization temperature of 1000 °C, all Zn species, including the semiconducting ZnO integrated into the porous carbon matrix, are removed, as confirmed by XPS and XRD analyses, resulting in a notable enhancement in electrical conductivity. This sharp increase is attributed to the improved graphitization and reduced structural disorder at this temperature, as confirmed by the decreased I_D/I_G ratio in the Raman spectra (Fig. S7), indicating a transition towards a more ordered carbon framework.

Section C. Electrochemical characterization

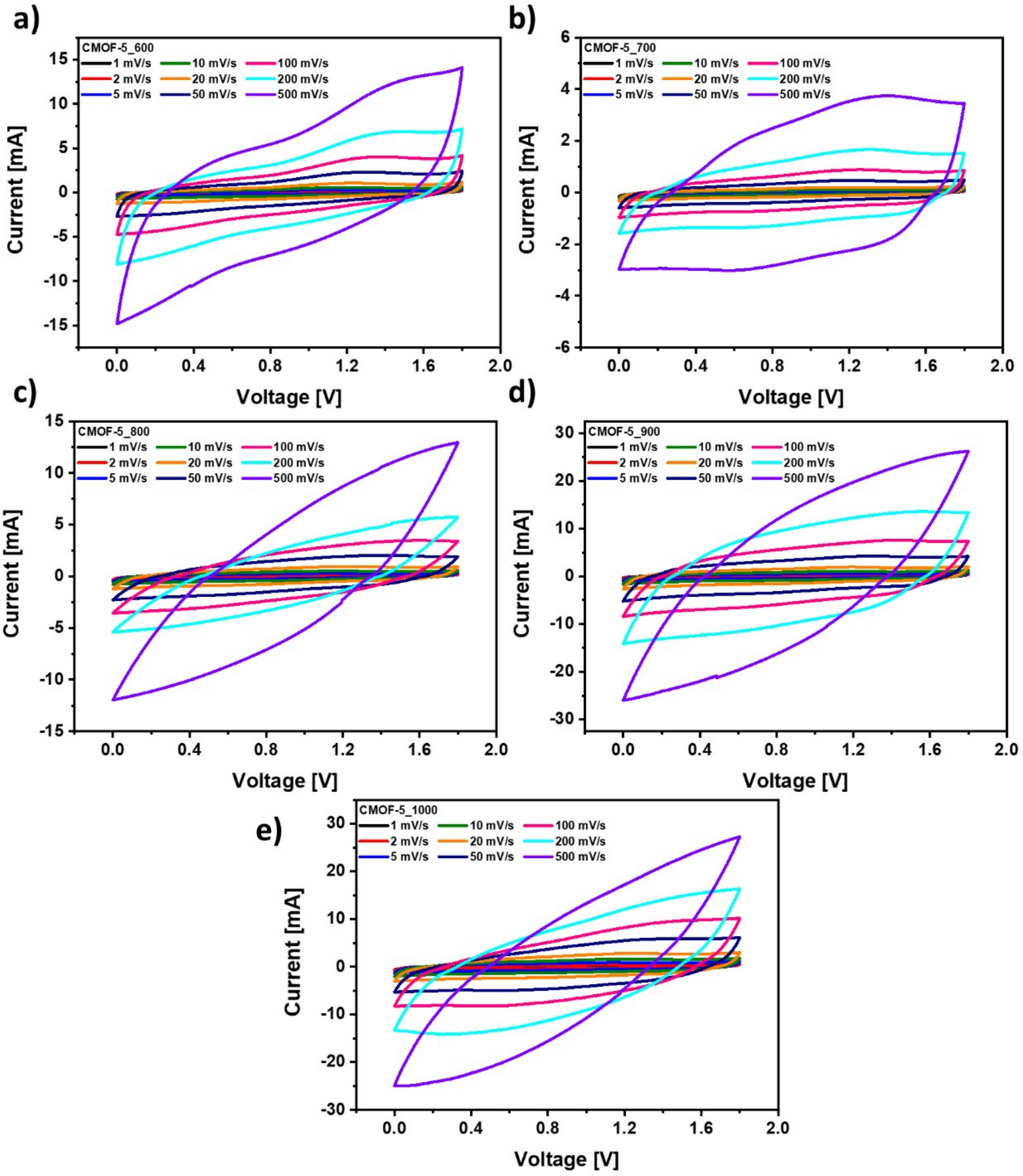

Fig. S10. CV curves of all CMOF-5 samples at different scan rates.

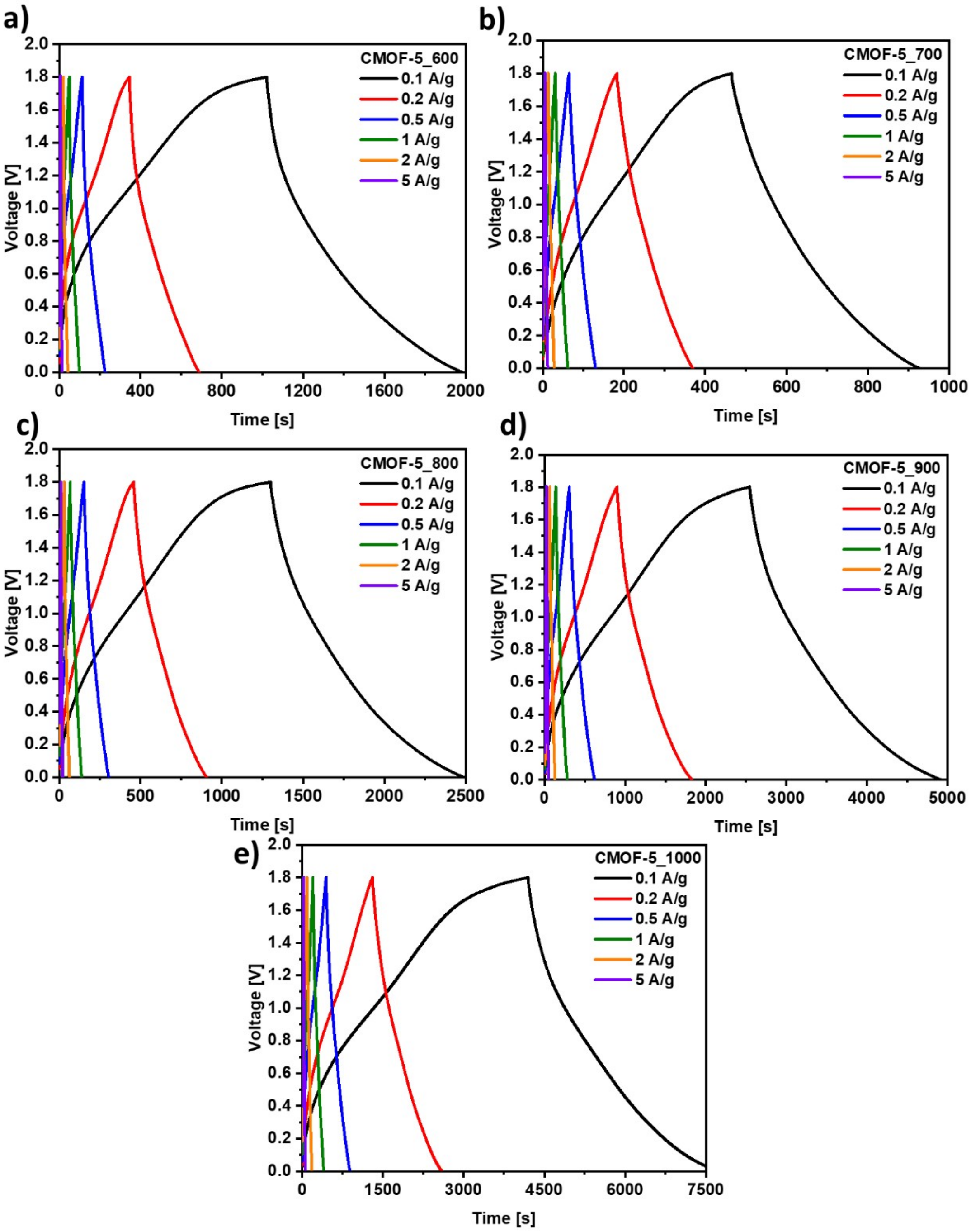

Fig. S11. GCD profiles of all CMOF-5 samples at different current densities.

Table S3. Physical parameters and maximum specific capacitance of the all obtained CMOF-5 samples.

Sample	**Ratio Zn/O**	**BET surface area [m^2/g]**	**Total pore volume [cm^3/g]**	**Electrical conductivity [S/m]**	**Specific capacitance [F/g]**
CMOF-5_600	0.57	443.80 ± 4.59	0.41	$3.24\ 10^{-5}$	133.51
CMOF-5_700	0.57	404.86 ± 4.18	0.41	$2.85\ 10^{-4}$	84.11
CMOF-5_800	0.83	420.12 ± 4.50	0.43	3.32	121.23
CMOF-5_900	0.72	919.06 ± 11.27	0.78	0.02	204.4
CMOF-5_1000	-	2151.07 ± 27.17	1.87	50.15	268.93

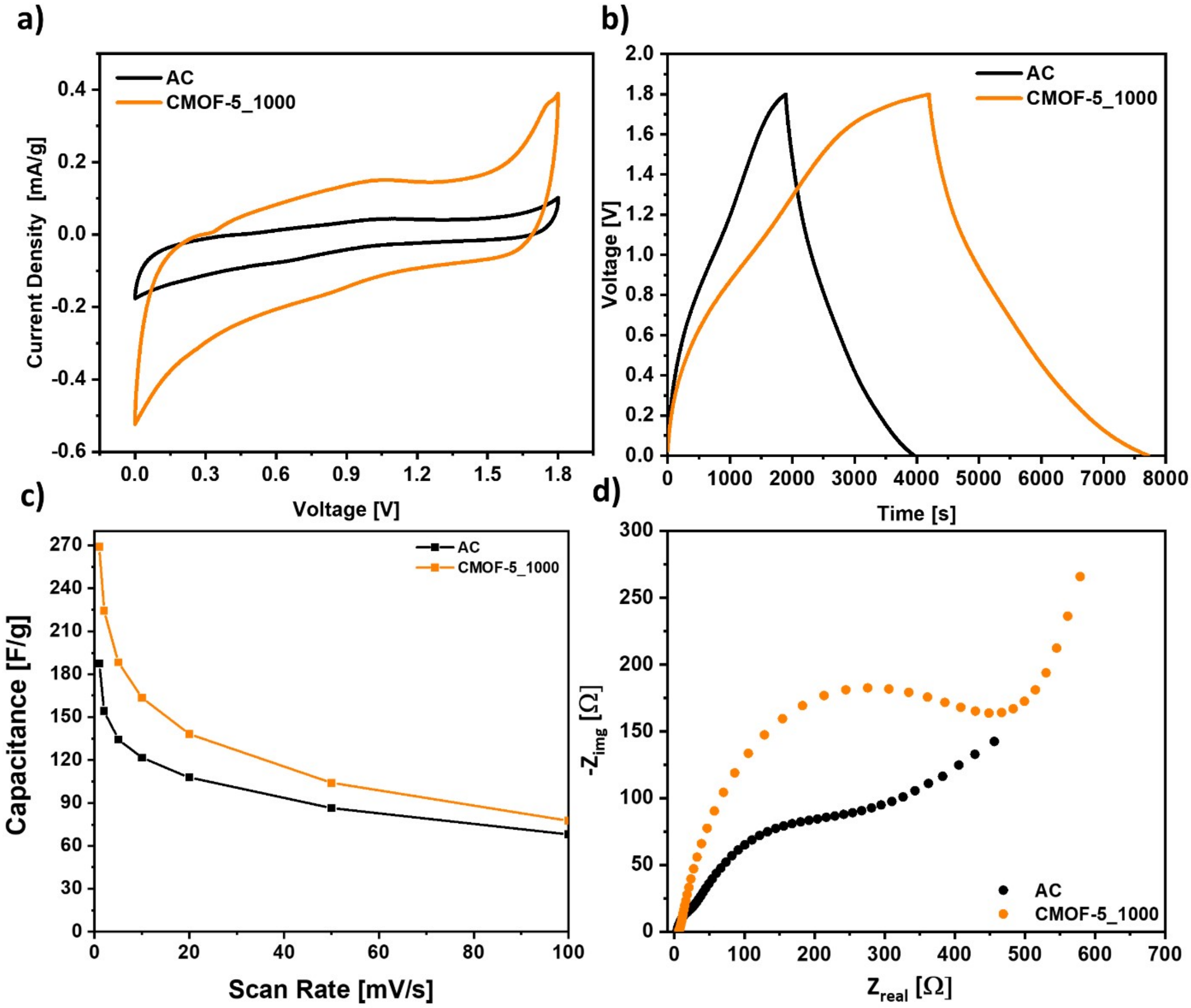

Fig. S12. a) CV curves at scan rate of 1 mV/s, b) GCD profiles at a current density of 0.1 A/g, c) capacitances at different scan rates and d) Nyquist plots of commercial AC and CMOF-5_1000 sample.

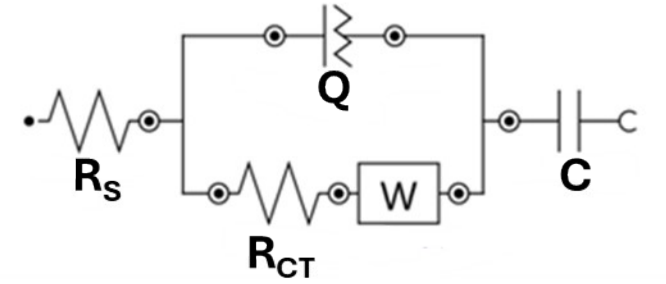

Fig. S13. The equivalent electric circuit models used for fitting the Nyquist plots.

R_S represents the total internal resistance, which includes the interfacial contact resistance between the material and the current collector, the ohmic resistance of the electrolyte, and the intrinsic resistance of the current collector. It can be determined from the high-frequency region of the Nyquist plot by its intersection with the real axis. R_{CT}, on the other hand, corresponds to the interfacial charge transfer resistance, which is indicated by the diameter of the semicircle and reflects the resistance associated with electrochemical reactions at the electrode surface. Additionally, the semicircle accounts for a constant phase element (Q) arising from the double-layer capacitance behavior. In the middle-frequency region, the sloped transmission line represents the Warburg element (W), which characterizes the transport and diffusion of electrons and electrolyte ions within the electrode material pores.

Table S4. Circuit parameters for the EIS measurements of CMOF-5.

Sample [°C]	**R_S [Ω]**	**R_{CT} [Ω]**
600	92	2437
700	13.88	1296
800	47.9	767
900	65.56	570.3
1000	6.738	488.4

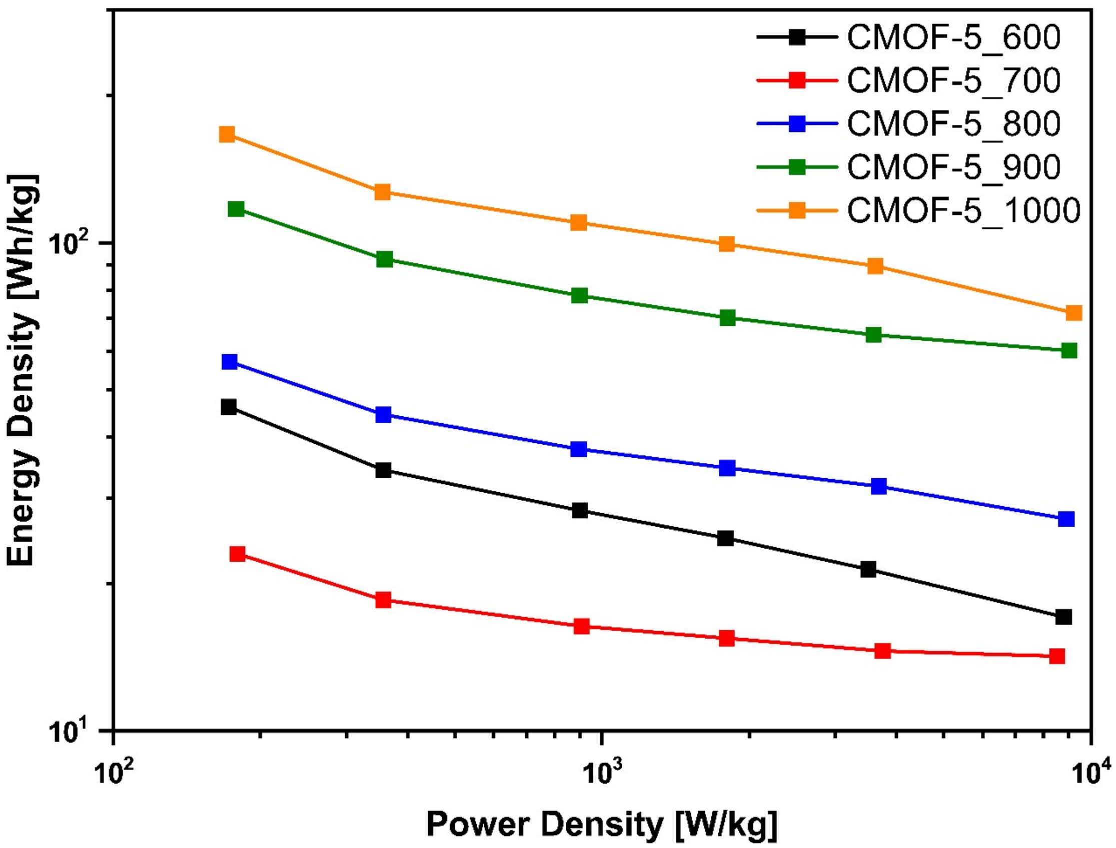

Fig. S14. Ragone Plot for all CMOF-5 samples.

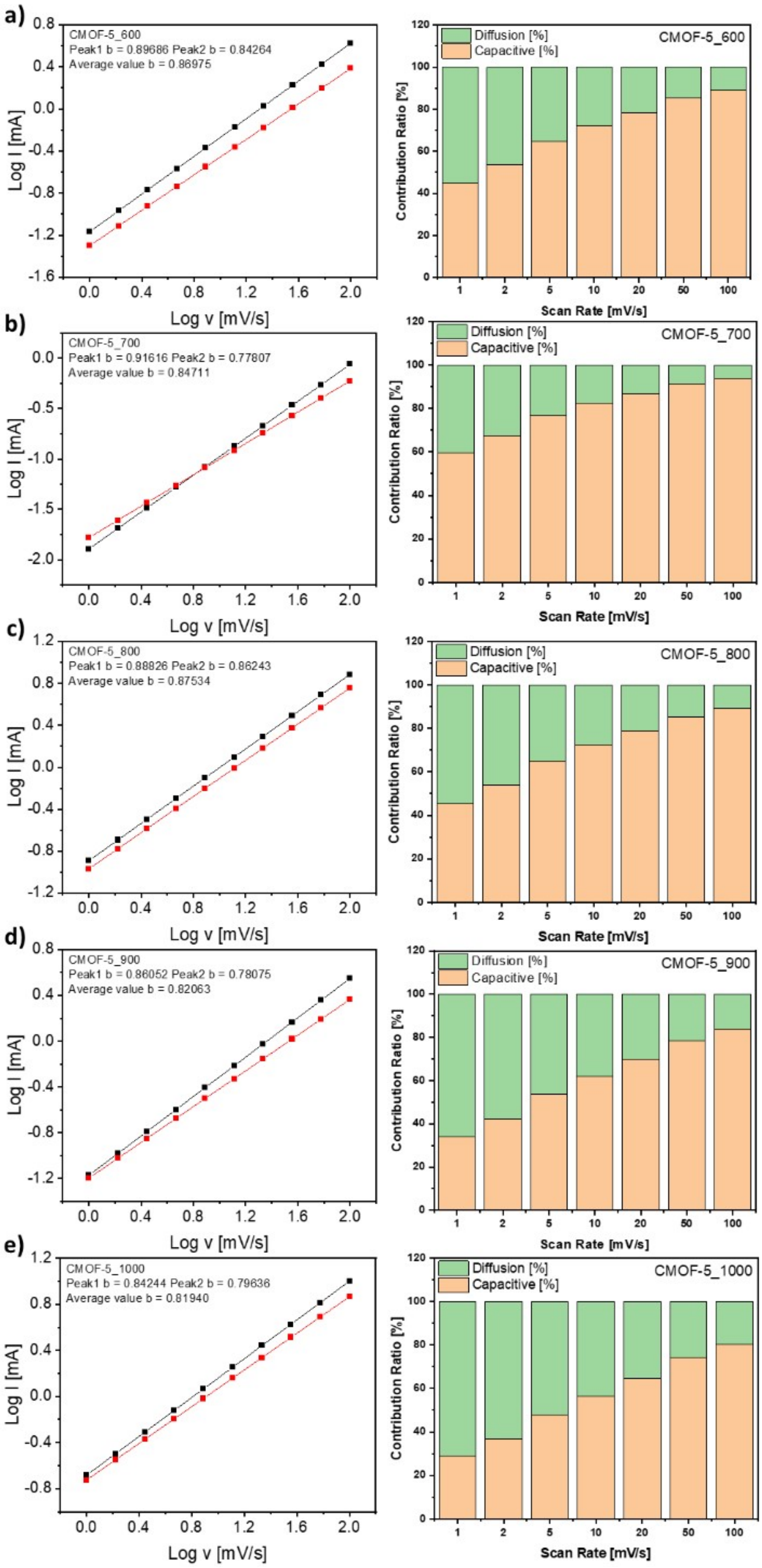

Fig. S15. Fitting plots between log(i) and log (v) at various peak currents. Capacitive (contribution) and diffusion-controlled contribution of all CMOF-5 samples at various scan rates.

Table S5. State of the art of the electrochemical performance of various cathode materials in Zn-ESS.

Cathode	***Electrolyte***	***Capacitance / Capacity***	***Current density or scan rate***	***Cyclability***	***Energy density***	***Power density***	***Surface area***	***Reference***
Carbon materials								
DFs	1 M $ZnSO_4$	35.1 F/g	0.2 A/g	89.9 % (10 000 cycles at 1 A/g)	70.7 Wh/kg	4395.3 W/kg	3068.48 m^2/g	[5]
oCNT	1 M $ZnSO_4$-PVA gel	53 F/g	10 mV/s	100 % (5 000 cycles at 500 mV/s)	-	-	211 m^2/g	[6]
C2NN1-800-1-5	2 M $ZnSO_4$	296.4 F/g	0.2 A/g	100 % (10 000 cycles at 6 A/g)	133.4 Wh/kg	18000 W/kg	1256 m^2/g	[7]
AC	2 M $ZnSO_4$	259.4 F/g	0.05 A/g	100 % (10 000 cycles at 1.56 mA/cm^2)	115.4 µWh $/cm^2$	0.16 mW/cm^2	1825 m^2/g	[8]
MXene-rGO	2 M $ZnSO_4$	128.6 F/g	0.4 A/g	95 % (75 000 cycles at 5 A/g)	34.9 Wh/kg	2800 W/kg	-	[9]
MPCs-3	1 M $Zn(CF_3SO_3)_2$	209 F/g	0.2 A/g	100 % (10 000 cycles at 2 A/g)	92.7 Wh/kg	7264 W/kg	2807 m^2/g	[10]
aMEGO	3 M $Zn(CF_3SO_3)_2$	210 F/g	0.1 A/g	93 % (80 000 cycles at 8 A/g)	106.3 Wh/kg	31400 W/kg	2957 m^2/g	[11]
RHC	3 M $Zn(CF_3SO_3)_2$	149.8 F/g	0.2 A/g	95.9 % (3005 cycles at 2 A/g)	58.6 Wh/kg	10000 W/kg	-	[12]
A-NOCNS	2 M $Zn(CF_3SO_3)_2$	176.48 mAh/g	0.2 A/g	90.2 % (20 000 cycles at 10 A/g)	162.8 Wh/kg	28.4 kW/kg	528.38 m^2/g	[13]
CS	3 M $Zn(CF_3SO_3)_2$	240 mAh/g	0.5 A/g	90.9 % (300 000 cycles at 50 A/g)	145 Wh/kg	-	1780 m^2/g	[14]
AC	1 M $Zn(CF_3SO_3)_2$	170 F/g	0.1 A/g	91 % (20 000 cycles at 2 A/g)	52.7 Wh/kg	1725 W/kg	3384 m^2/g	[15]
MOF-derived materials								
MDC	1 M $ZnSO_4$	123 F/g	0.2 A/g	99 % (20 000 cycles at 1 A/g)	7.5 Wh/kg	85000 W/kg	270 m^2/g	[16]
ZDC	2 M $ZnSO_4$	341 F/g	0.5 A/g	75 % (20 000 cycles at 1 A/g)	121.2 Wh/kg	16000 W/kg	551.3 m^2/g	[17]
MPC	3 M $Zn(CF_3SO_3)_2$	289.2 F/g	0.2 A/g	96.7 % (10 000 cycles at 10 A/g)	130.1 Wh/kg	7800 W/kg	2125 m^2/g	[18]
CMOF-5_600	3 M $Zn(CF_3SO_3)_2$	133.51 F/g 20.1 mAh/g	1 mV/s 0.1 A/g	52 % (10 000 cycles at 1 A/g)	46.1 Wh/kg	8794 W/kg	444 m^2/g	this work
CMOF-5_700	3 M $Zn(CF_3SO_3)_2$	84.11 F/g 10.7 mAh/g	1 mV/s 0.1 A/g	88 % (10 000 cycles at 1 A/g)	23.0 Wh/kg	8532 W/kg	405 m^2/g	this work
CMOF-5_800	3 M $Zn(CF_3SO_3)_2$	121.23 F/g	1 mV/s	83 %	57.1 Wh/kg	8895 W/kg	420 m^2/g	this work

		26.4 mAh/g	0.1 A/g	(10 000 cycles at 1 A/g)				
CMOF-5_900	3 M $Zn(CF_3SO_3)_2$	204.4 F/g 54.8 mAh/g	1 mV/s 0.1 A/g	84 % (10 000 cycles at 1 A/g)	117.4 Wh/kg	9018 W/kg	919 m^2/g	this work
CMOF-5_1000	**3 M $Zn(CF_3SO_3)_2$**	**268.93 F/g** **73.7 mAh/g**	**1 mV/s** **0.1 A/g**	**88 %** **(10 000 cycles at 1 A/g)**	**166.9 Wh/kg**	**9234 W/kg**	**2151 m^2/g**	**this work**

Where: DFs – diamond fibers, oCNT - oxidized carbon nanotubes, *C2NN1-800-1-5* - chitin-derived NaCl-templated and $NaNO_3$-activated carbon, AC – activated carbon, MPCs – mesoporous carbons aMEGO - porous carbon derived from chemical activated graphene, RHC – rice husk deribed carbon, MDC – MOF derived carbon, ZDC - ZIF-8 derived N-doped porous carbon, MPC - MIL-47-derived porous carbon, A-NOCNS - ultra-thin N-doped oxygen-rich porous carbon nanosheets, CS - carbon superstructures.

It is important to note that the comparative analysis presented here is intended as a general benchmarking across state-of-the-art Zn-ion storage materials. While differences in electrolyte composition and testing protocols exist among the referenced studies, the comparison highlights overall performance trends and emphasizes the favourable balance of energy and power density achieved by CMOF-5_1000 under our specific operating conditions.

References

1 K. Cendrowski, P. Skumial, P. Spera and E. Mijowska, *Mater. Des.*, 2016, **110**, 740–748.
2 S. J. Yang, T. Kim, J. H. Im, Y. S. Kim, K. Lee, H. Jung and C. R. Park, *Chem. Mater.*, 2012, **24**, 464–470.
3 M. Fiaz, M. Kashif, M. Fatima, S. R. Batool, M. A. Asghar, M. Shakeel and M. Athar, *Catal. Lett.*, 2020, **150**, 2648–2659.
4 Y. H. Hu and L. Zhang, *Phys. Rev. B*, 2010, **81**, 174103.
5 Z. Jian, N. Yang, M. Vogel, S. Leith, A. Schulte, H. Schönherr, T. Jiao, W. Zhang, J. Müller, B. Butz and X. Jiang, *Adv. Energy Mater.*, 2020, **10**, 2002202.
6 Y. Tian, R. Amal and D.-W. Wang, *Front. Energy Res.*, DOI:10.3389/fenrg.2016.00034.
7 H. Yu, X. Chen, J. Zhou and H. Wang, *J. Mater. Sci. Mater. Electron.*, 2023, **34**, 675.
8 P. Zhang, Y. Li, G. Wang, F. Wang, S. Yang, F. Zhu, X. Zhuang, O. G. Schmidt and X. Feng, *Adv. Mater.*, 2019, **31**, 1806005.
9 Q. Wang, S. Wang, X. Guo, L. Ruan, N. Wei, Y. Ma, J. Li, M. Wang, W. Li and W. Zeng, *Adv. Electron. Mater.*, 2019, **5**, 1900537.
10 C. Jiang and Z. Zou, *Diam. Relat. Mater.*, 2020, **101**, 107603.
11 S. Wu, Y. Chen, T. Jiao, J. Zhou, J. Cheng, B. Liu, S. Yang, K. Zhang and W. Zhang, *Adv. Energy Mater.*, 2019, **9**, 1902915.
12 Y. Liu, H. Tan, Z. Tan and X. Cheng, *Appl. Surf. Sci.*, 2023, **608**, 155215.
13 Y. Han, C. Zhang, K.-J. Chen and T. Wang, *J. Mater. Chem. A*, 2024, **12**, 24296–24307.
14 Q. Huang, L. Huang, Y. Jin, Y. Sun, Z. Song and F. Xie, *Chem. Eng. J.*, 2024, **482**, 148912.
15 H. Wang, M. Wang and Y. Tang, *Energy Storage Mater.*, 2018, **13**, 1–7.
16 T. Xiong, Y. Shen, W. S. V. Lee and J. Xue, *Nano Mater. Sci.*, 2020, **2**, 159–163.
17 Y. Wei, X. Chen, G. Gao, D. Shen, H. Rong and Q. Liu, *Ionics*, 2022, **28**, 3477–3488.
18 H. Li, J. Wu, L. Wang, Q. Liao, X. Niu, D. Zhang and K. Wang, *Chem. Eng. J.*, 2022, **428**, 131071.